JOURNAL OF SOLID STATE CHEMISTRY **132,** 274–283 (1997)
ARTICLE NO. SC977442

Compounds and Phase Relations in the SrO–CaO–CuO System under High Pressure

Naoya Kobayashi,* Zenji Hiroi, and Mikio Takano

Institute for Chemical Research, Kyoto University, Uji, Kyoto-fu 611, Japan

Received January 30, 1996; in revised form November 18, 1996; accepted April 22, 1997

The phase relation in the ternary SrO–CaO–CuO system under high pressure has been studied by means of powder X-ray diffraction, electron diffraction, and high-resolution electron microscopy. In the SrO–CuO system studied in a pressure and temperature range of 1.7–8 GPa and 850–1150°C, Sr_2CuO_3, $SrCuO_2$(II), $Sr_2Cu_3O_5$, and $SrCu_2O_3$ form. In the CaO–CuO system, $CaCuO_2$ (I) of the infinite-layer type forms at 3–5 GPa and 1050–1200°C. This compound undergoes a polymorphic structural transformation into another high-pressure form $CaCuO_2$ (II) which comprises a new type of CuO_2 planes. A structural model built on the basis of electron diffraction and high-resolution electron microscopy is presented. The ternary phase diagram at 4 GPa and 1020°C is presented. © 1997 Academic Press

INTRODUCTION

In the search for new high-T_c superconductors, many ternary and quarternary systems including CuO as one of the components have been explored. Cupric oxide superconductors generally consist of single two-dimensional (2D) CuO_2 planes or multiple CuO_2 planes stacked as CuO_2/M/CuO_2 (M, relatively small alkaline-earth metal ions or rare-earth metal ions), and charge-reservoir layers in which specific metals or molecules such as La, Bi, Tl, Hg, and CO_3 distinguishing one system from the other are included.

The most commonly included metal elements in cupric oxide superconductors are apparently alkaline-earth metals (A), Ba, Sr, and Ca. The study of the A–Cu–O system is important not only for the purpose of searching for new high-T_c superconductors having simple compositions and simple structures but also for the purpose of understanding the fundamental crystal chemistry of cupric oxide superconductors. The ternary SrO–CaO–CuO system has been studied by many groups. In the subsolidus phase diagram at $\sim$1000°C and ambient pressure (1–4), five compounds or solid solutions were found: $(Sr_{1-x}Ca_x)_2CuO_3$ ($0 \le x \le 1$) (5), $Sr_{1-x}Ca_xCuO_2$ ($0 \le x \le 0.75$) (6), $Sr_{1-x}Ca_xCuO_2$ ($0.86 \le x \le 0.9$) (7,8), $Ca_{1-x}CuO_2$ ($x \sim 0.15$) (9), and $(Sr_{1-x}Ca_x)_{14}Cu_{24}O_{41}$ ($0 \le x \le 0.5$) (10). It is interesting to notice that these materials have served for the study of low-dimensional physics, because they comprise various low-dimensional networks made of CuO_4 planar squares such as single linear Cu–O chains made by corner-sharing ($(Sr_{1-x}Ca_x)_2CuO_3$), double Cu–O chains bound together by edge-sharing ($Sr_{1-x}Ca_xCuO_2$), another type of single chains made of edge-sharing CuO_4 squares ($(Sr_{1-x}Ca_x)_{14}Cu_{24}O_{41}$ and $Ca_{0.85}CuO_2$), and 2D CuO_2 planes in $Sr_{1-x}Ca_xCuO_2$ ($0.86 \le x \le 0.91$) which crystallizes in the extremely simple infinite layer (IL) structure.

Application of high pressure is known to change phases and their relations dramatically in various systems. Such high-pressure effects on complex cupric oxides were first demonstrated in the stabilization of the IL structure for $ACuO_2$ over a wide range of alkaline-earth metal compositions (11). A new homologous series of compounds with the general formula $Sr_{n-1}Cu_nO_{2n-1}$ (12) were isolated for $n = 2$ and 3 at 6 GPa. These contain a specific 2D Cu_nO_{2n-1} sheet which can be derived by shearing a regular CuO_2 sheet so that double CuO chains such as those found in the ambient-pressure phase of $SrCuO_2$ form periodically. $Sr_{n-1}Cu_nO_{2n-1}$ has been considered to be a good model compound for the physical spin–ladder model from which intriguing quantum phenomena including superconductivity can be expected (13). The high-pressure synthesis technique can thus lead us to new low-dimensional systems.

In the present study, we have investigated the phase relation in the SrO–CaO–CuO system treated up to 8 GPa and 1250°C. The three high-pressure Sr–Cu–O phases, which were prepared at 6 GPa previously, have been found to be stable at $1.5 \le P \le 8$ GPa, while the phase relation in the CaO–CuO system varies sensitively with pressure. $CaCuO_2$(I) of the IL type undergoes a transformation into another 2D structure containing a novel type of the CuO_2 plane at $\sim$4.5 GPa (1050°C). The stability of these phases as a function of pressure and composition will be presented.

* To whom correspondence should be addressed.

0022-4596/97 $25.00

EXPERIMENTAL

Starting materials used for high-pressure syntheses were CuO, CaO, SrO, $CaCu_2O_3$, $SrCuO_2$, and appropriate mixtures of these compounds. The binary compounds were prepared in advance by ordinary solid-state reactions from $SrCO_3$, $CaCO_3$, and CuO (99.9% pure each). For example, $CaCu_2O_3$ and CaO were mixed at a molar ratio of 1 : 1 to obtain a "$CaCuO_2$" composition. The combination of CuO and Ca_2CuO_3, or Sr_2CuO_3, was not useful because these were not very reactive with each other. They were sealed in cylindrical gold capsules 3 mm in diameter and 3 mm in height, pressed almost isostatically up to a certain pressure between 1.7 and 8 GPa using a cubic-anvil-type high-pressure apparatus, and then heat-treated at 850–1200°C for 30 min. Details of the high-pressure cell assembly were described previously (14). The temperature was monitored with a Pt–PtRh thermocouple placed near the gold capsule. The actual sample temperature was assumed to be higher by 50°C than monitored because the thermocouple was anchored at a pair of anvils typically warmed up to 50°C. Thus, the reliability of the absolute sample temperature was not very good. After the heat treatment, the same was quenched to room temperature, and then the pressure was released gradually.

The obtained samples were characterized by means of powder X-ray diffraction (XRD), electron diffraction (ED), and high-resolution electron microscopy (HREM). The XRD measurements were performed on a Rigaku rotating-anode diffractometer with graphite-monochromatized Cu$K\alpha$ radiation. Lattice parameters were refined using the Rietveld software Rietan working on a Macintosh computer (15). Data for the Rietveld analysis were collected at room temperature over a 2θ range of 16–120° at a 0.03° step for 10 s each. The ED and HREM experiments were carried out on a JEOL-2000EX electron microscope equipped with a top-entry goniometer stage operating at 200 kV. A specimen for the observation was prepared by crushing a pellet in acetone and collecting fragments on a carbon-coated holey film supported by a copper grid. Simulations of HREM images were made using MacTempus software. Chemical analysis using an energy-dispersive X-ray analysis (EDX) technique was carried out for some samples. Thermal gravimetry (TG) and differential thermal analysis (DTA) were done to study the stability of the high-pressure products at ambient pressure.

RESULTS AND DISCUSSION

The SrO–CuO System

In the SrO–CuO system, Sr_2CuO_3, $SrCuO_2$(I), and $Sr_{14}Cu_{24}O_{41}$ are known to exist at ambient pressure. Among them, only Sr_2CuO_3 survives up to 8 GPa. $Sr_{14}Cu_{24}O_{41}$ is not expected to appear in the present experiments in which the nominal Cu valence was kept at 2+ in a closed system. The transformation of $SrCuO_2$(I) into $SrCuO_2$(II) crystallizing in the IL structure takes place at a critical pressure between 1.5 and 3 GPa at 1000°C. The composition–temperature section determined at 3 GPa is shown in Fig. 1. Essentially the same phase relations were found at 6 and 8 GPa.

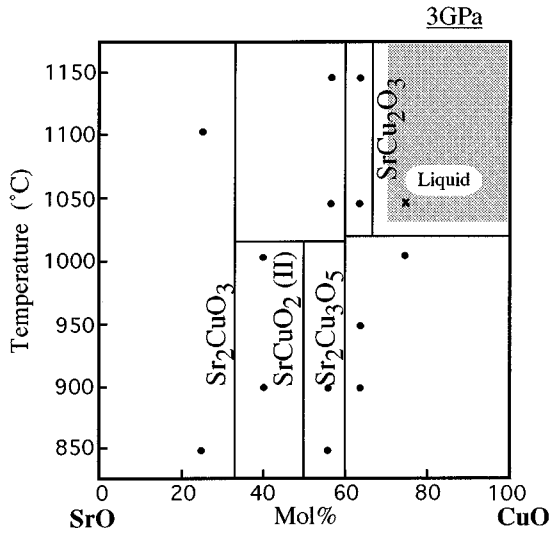

FIG. 1. The SrO–CuO pseudo binary phase diagram at 3 GPa.

$SrCu_2O_3$, $Sr_2Cu_3O_5$, and $SrCuO_2$(II) are the members of a homologous series $Sr_{n-1}Cu_nO_{2n-1}$ with $n = 2$, 3, and ∞, respectively.[1] Their XRD patterns are shown in Fig. 2, and structural data are summarized in Table 1. $SrCuO_2$(II) decomposes into Sr_2CuO_3 and $Sr_2Cu_3O_5$ at about 1025°C. $Sr_2Cu_3O_5$ is stable for the whole temperature range examined, while $SrCu_2O_3$ appears only at high temperatures above 1000°C. Other members with $n \geq 4$ were not detected in the present XRD measurements, though they were occasionally seen electron microscopically to be intergrown with the $n \leq 3$ members (12). The $n \geq 4$ members might be obtainable at relatively low temperatures if one would start from oxide precursors in which the constituent metals were atomically mixed.

Partial melting and reactions with gold capsules prevented us from investigating the Cu-rich region with $Sr/Cu < 1/2$ at high temperatures. No new phases were found in the Sr-rich region with $Sr/Cu > 2$. The previously reported homologous series of compounds with the general formula $Sr_{n+1}Cu_nO_{2n+1+\delta}$ (16) did not appear because of the inert, nonoxidizing atmosphere.

[1]The general formula $Sn_{n-1}Cu_{n+1}O_{2n}$ was used for the homologous series of compounds in the previous work (12). In this report, however, we take a simpler and more meaningful formula $Sr_{n-1}Cu_nO_{2n-1}$, where $n = 1$, 2, 3, and ∞ means CuO, two-leg ladder compound $SrCu_2O_3$, three-leg ladder compound $Sr_2Cu_3O_5$, and IL-$SrCuO_2$, respectively.

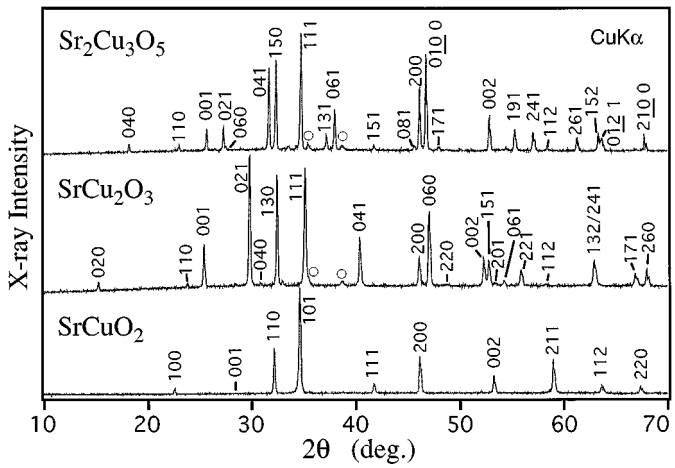

FIG. 2. XRD profiles of three high-pressure phases; $Sr_2Cu_3O_5$, $SrCu_2O_3$, and $SrCuO_2$ (II). The peaks marked with ○ come from CuO.

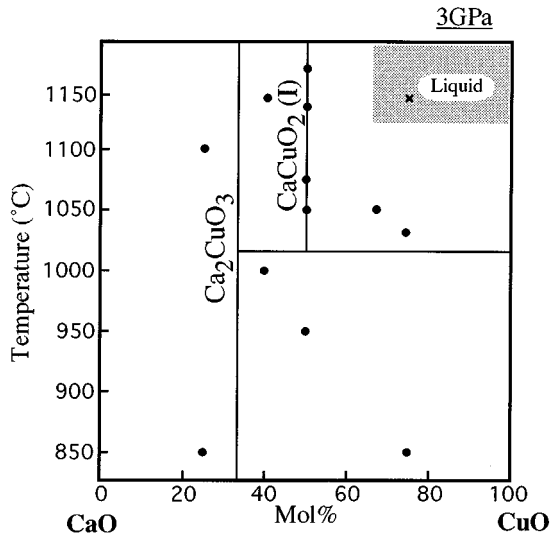

FIG. 3. The CaO–CuO pseudo binary phase diagram at 3 GPa. The IL-type $CaCuO_2$ (I) phase appears above 1025°C.

The CaO–CuO System

The phase relation in the CaO–CuO system has been found to be more sensitive to pressure than that in the SrO–CuO system. Two Cu^{2+} compounds are known in this system at ambient pressure: Ca_2CuO_3 (6) and $CaCu_2O_3$ (17). The former is isomorphous with Sr_2CuO_3. The latter is structurally related to $SrCu_2O_3$ in a sense that both of them contain Cu_2O_3 layers, though the layers in $CaCu_2O_3$ are heavily corrugated. Another compound, $Ca_{0.85}CuO_2$ (18), has a nominal Cu valence of 2.3 and so is not expected to appear in the present experiments. Figure 3 illustrates the temperature-composition section determined at 3 GPa. Ca_2CuO_3 is quite stable, while $CaCu_2O_3$ decomposes into Ca_2CuO_3 and CuO at high pressure. Above 1000°C a new phase $CaCuO_2$(I) appears, which is isomorphous with IL-$SrCuO_2$(II). The XRD pattern is shown in Fig. 4. $CaCuO_2$ of the IL-type was previously prepared at a high-Ar-gas pressure of 0.1 GPa (19).

As pressure is further increased, a new phase appears at Ca/Cu ~ 1/1. Figure 5 shows a series of XRD profiles as a function of pressure. The profile obtained at 3.5 GPa and 1100°C is ascribed to the IL-type tetragonal cell, while extra peaks grow with increasing pressure to 4.0 GPa, and finally the IL-phase disappears completely at 4.5 GPa. The product at 4.5 GPa is not single-phase but includes one major and one minor, or possibly more, unknown phases and a small amount of CuO. We could not isolate these phases, though various combinations of experimental conditions of pressure, composition, and temperature were examined: The increase in CuO or CaO content in the starting material simply resulted in the increase in CuO or Ca_2CuO_3, respectively. Changing the synthesizing temperature did not significantly affect the relative amounts of the major phase and the secondary phases. A chemical analysis using EDX on

TABLE 1
High-Pressure Phases in the SrO–CaO–CuO System

	$SrCuO_2$(II)	$CaCuO_2$(I)	$SrCu_2O_3$	$Sr_2Cu_2O_3$	$CaCuO_2$(II)
Crystal system	Tetragonal	Tetragonal	Orthorhombic	Orthorhombic	Monoclinic
Space group	*P*4/*mmm* (No. 123)	*P*4/*mmm* (No. 123)	*Cmmm* (No. 65)	*Cmmm* (No. 65)	$P2_1$ (No. 4)
Z	1	1	2	2	4
a (Å)	3.9269(2)	3.8526(3)	3.9299(5)	3.9301(1)	5.4150(4)
b (Å)			11.5615(4)	19.4016(5)	10.7079(1)
c (Å)	3.4346(2)	3.1766(3)	3.4926(1)	3.4605(1)	3.1501(2)
β (deg.)					90.886(7)
Volume (Å^3)	52.953	47.149	159.121	263.973	182.631
Density (g/cm^3)	5.7449	4.7784	5.5002	5.6141	4.9599
Decomposition temperature (°C)[a]	400	≥ 900	560	450	

[a]Measurements were made in air at ambient pressure.

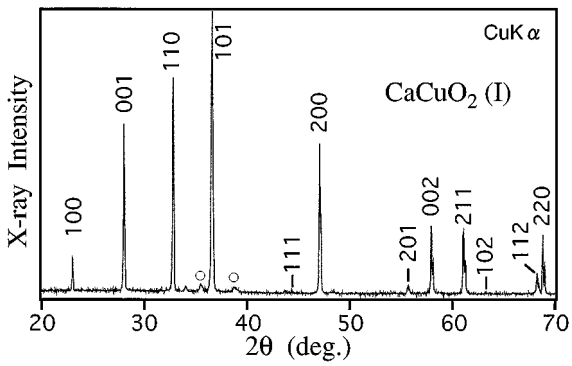

FIG. 4. XRD profile of $CaCuO_2$ (I) which is isomorphous with IL-$SrCuO_2$ (II). The peaks marked with ○ come from CuO.

many particles always indicated that Ca/Cu ~ 1. Thus, we have assumed that the major phase is a high-pressure form of $CaCuO_2$, which will be referred to hereafter as $CaCuO_2$(II). The presence of impurities with Ca/Cu ~ 1 compositions might have come from such factors as the locally nonhydrostatic nature of the pressure used and, more probably, the kinetics of reaction. If the quenching speed is not high enough, unstable low-temperature polymorphs of $CaCuO_2$ might form during the quenching.

The temperature–pressure section at Ca/Cu = 1 is shown in Fig. 6. Phase I is confined in a low-pressure and high-temperature region, while Phase II is stable in a more extended high-temperature and high-pressure region. As mentioned above, the unknown secondary phase(s) always exists in the region for Phase II. No other new phases were detected up to 8 GPa for any compositions.

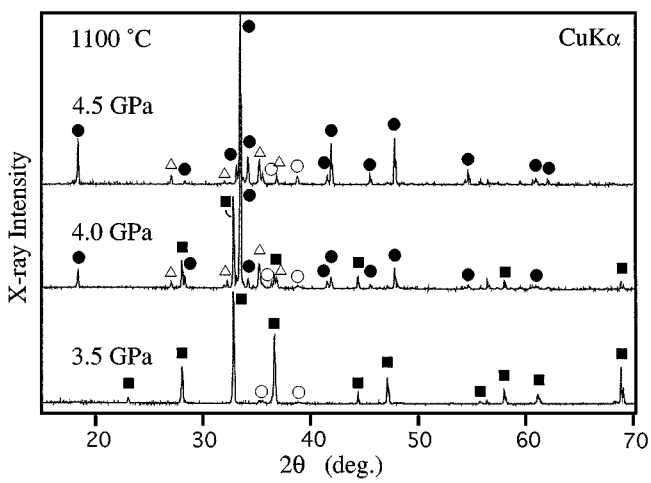

FIG. 5. XRD profiles for samples with Ca/Cu = 1 as a function of synthesis pressure at 1100°C (■, IL-$CaCuO_2$ (I); ●, $CaCuO_2$ (II); △, unknown phase; ○, CuO). IL-$CaCuO_2$ (I) which forms below 4 GPa transforms into a new high-pressure phase $CaCuO_2$ (II) above 4 GPa.

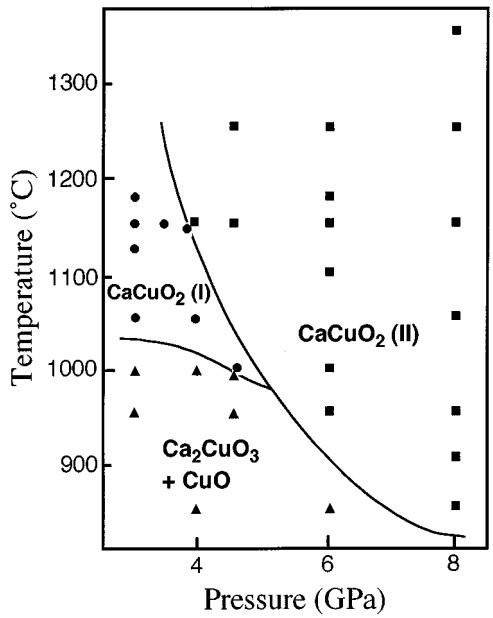

FIG. 6. Temperature–pressure section for Ca/Cu = 1. The $CaCuO_2$ (I) phase forms in a low pressure region, whereas $CaCuO_2$ (II) at higher pressures and higher temperatures.

The SrO–CaO–CuO System

The ternary phase diagram determined at 4 GPa at 1020°C is shown in Fig. 7. Approximately 30 compositions were examined. The system includes four solid-solution series: $(Sr_{1-x}Ca_x)_2CuO_3$ $(0 \le x \le 1)$, $Sr_{1-x}Ca_xCuO_2$ (IL) $(0 \le x \le 1)$, $(Sr_{1-x}Ca_x)_2Cu_3O_5$ $(0 \le x \le 0.3)$, and $(Sr_{1-x}Ca_x)Cu_2O_3$ $(0 \le x \le 0.15)$. Only the first series is seen in the phase diagram made at ambient pressure.

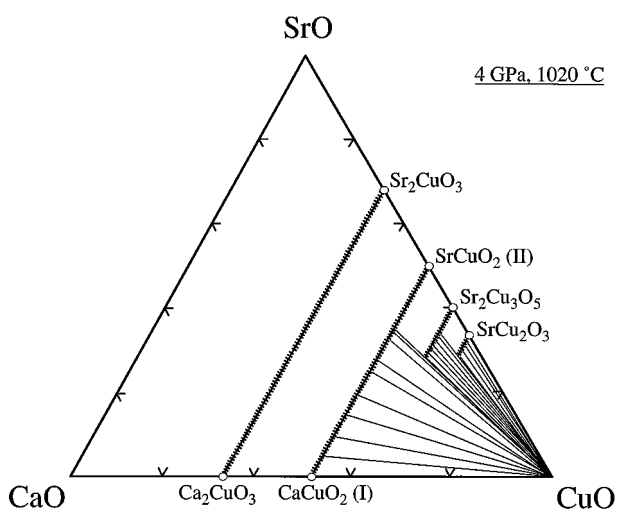

FIG. 7. Phase relations of the SrO–CaO–CuO ternary system at 4 GPa and 1020°C. Four solid-solution series exist.

The second IL series extends all the way between the two end members. The composition dependences of the lattice parameters are shown in Fig. 8. Both the a and c axes increase linearly with increasing Sr content, straightforwardly reflecting the increase in the average A-ion size. The fitted lines in the figure follow the equations

$$a(\text{Å}) = 3.928(8) - 0.079(3)x$$

$$c(\text{Å}) = 3.434(2) - 0.258(5)x.$$

The previously reported values for $Sr_{0.14}Ca_{0.86}CuO_2$ ($a = 3.8611$ Å, $c = 3.1995$ Å) and for $CaCuO_2$ ($a = 3.8556$ Å, $c = 3.1805$ Å) (20) approximately fall on the lines. It is noted that the a-axis length which corresponds to the Cu–Cu separation in the CuO_2 layers covers a wide range between ~ 3.85 Å ($A = $ Ca) and ~ 3.93 Å ($A = $ Sr), which are typical distances for hole-doped and electron-doped superconductors such as $YBa_2Cu_3O_7$ and $Nd_{1.85}Ce_{0.15}CuO_4$, respectively.

The phase stability of $ACuO_2$ has further been investigated as a function of pressure. The pressure-composition section for $A/Cu = 1$ at 1000–1050°C is shown in Fig. 9. $SrCuO_2$(I) is stable at 2 GPa but is replaced by $SrCuO_2$(II) at higher pressures. The critical pressure seems to decrease with increasing Ca content to reach ambient pressure at $x \sim 0.85$. For $A = $ Ca, on the other hand, the IL-type $CaCuO_2$(I) appears only for $1.5 \leq P \leq 4$ GPa and transforms into $CaCuO_2$(II) above 4 GPa. The phase boundary rises with increasing Sr content. The IL structures is stable for $0 \leq x \leq 0.85$ at 8 GPa.

The composition dependences of the lattice parameters for $(Sr_{1-x}Ca_x)_2Cu_3O_5$ and $(Sr_{1-x}Ca_x)Cu_2O_3$ are shown in Fig. 10. All the lattice dimensions decrease with increasing Ca content for both series. The solubility limit is smaller for $SrCu_2O_3$ than for $Sr_2Cu_3O_5$. Beyond the limit, $(Sr_{1-x}Ca_x)Cu_2O_3$ is dissociated into CuO and $(Sr_{1-x}Ca_x)_2Cu_3O_5$, and $(Sr_{1-x}Ca_x)_2Cu_3O_5$ into CuO and the IL-type $Sr_{1-x}Ca_xCuO_2$ as shown in the ternary phase diagram of Fig. 7.

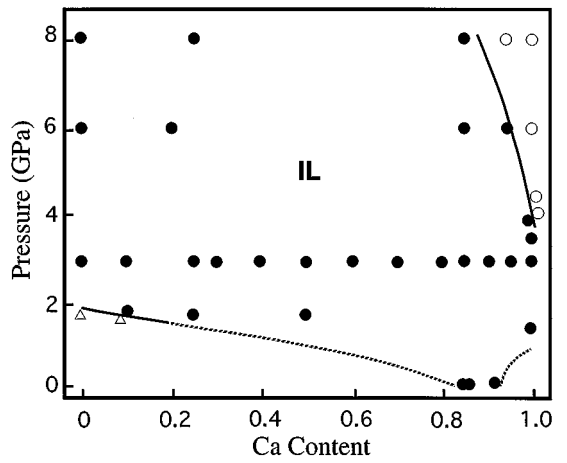

FIG. 9. Pressure–composition section for $A/Cu = 1$ at 1050°C. ●, IL-type phase; ○, Ca(Sr)CuO_2 (II); and △, Sr(Ca)CuO_2 (I).

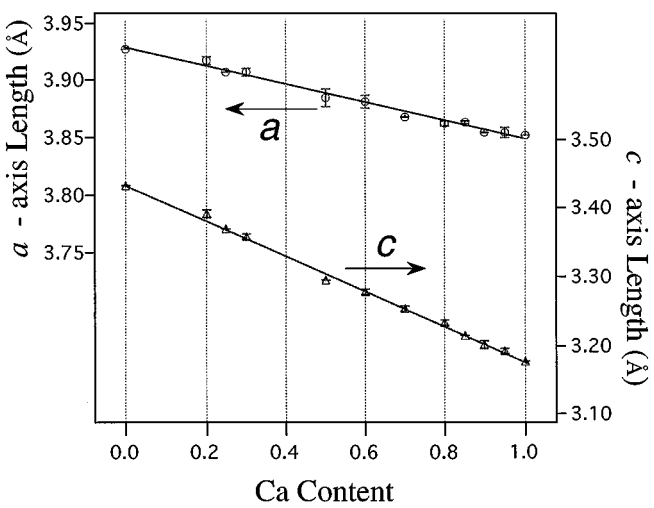

FIG. 8. Composition dependence of the lattice parameters for $Sr_{1-x}Ca_xCuO_2$ of the IL type. Both a and c axes decrease linearly with decreasing average A-ion size.

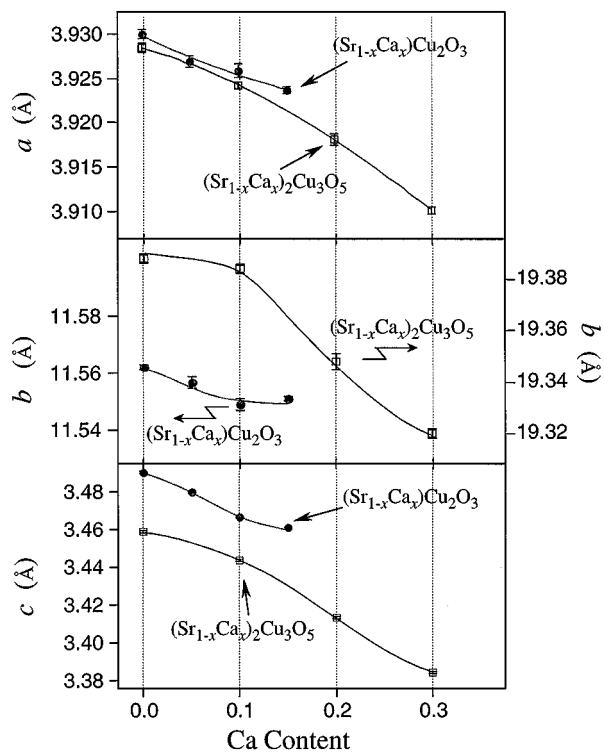

FIG. 10. Lattice parameters as a function of Ca content for $(Sr_{1-x}Ca_x)Cu_2O_3$ and $(Sr_{1-x}Ca_x)_2Cu_3O_5$.

Stability of High-Pressure Phases

To discuss the phase stability under high pressure it is generally significant to compare the density of a high-pressure phase with that of the corresponding ambient-pressure phase or phase mixtures. Figure 11 compares the calculated density of "$ACuO_2$" as a function of A composition. It is found that the high-pressure IL phase is always denser by $\sim 7.5\%$ for $x \leq 0.8$. In the case of $A = Ca$ ($x = 1$), on the other hand, the density of the IL phase is only slightly larger than that of the 1:1 assemblage $Ca_2CuO_3 + CuO$, which suggests that the synthesis under high pressure is not so critical for $A = Ca$. This is reflected in the fact that $CaCuO_2$(I) remains stable up to 900°C in air, while $SrCuO_2$(II) decomposes at a much lower temperature as shown in the next paragraph. One of the reasons $CaCuO_2$(I) cannot be prepared at ambient pressure is considered to be the low melting temperature at the composition. The increase in the melting temperature under high pressure can result in the appearance of the hidden phase.

High-pressure phases are apparently metastable at ambient pressure. However, quenchable high-pressure phases usually keep their form at room temperature for a practically long period, which is in fact the case for the present high-pressure products. The metastability at ambient pressure and elevated temperature was studied by XRD measurements after annealing at fixed temperatures for 12 h. $SrCuO_2$(II) transforms in $SrCuO_2$(I) at 400°C. $Sr_2Cu_3O_5$ and $SrCu_2O_3$ begin decomposing into a mixture of $Sr_{14}Cu_{24}O_{41}$ and CuO at 450 and 560°C, respectively. The decomposition is accompanied by a weight gain as measured by TG-DTA analysis due to the partial oxidation to $Sr_{14}Cu_{24}O_{41}$. The decomposition temperatures are summarized in Table 1.

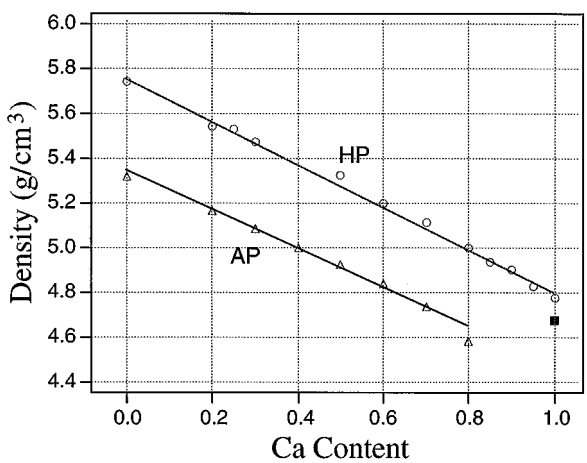

FIG. 11. Density as a function of Ca content for $Sr_{1-x}Ca_xCuO_2$. The HP phase of the IL type is always denser than the AP phase or phase mixtures. The mark ■ represents the density of a 1:1 assemblage of Ca_2CuO_3 and CuO.

Structure of $CaCuO_2$(II)

The crystal structure of $CaCuO_2$(II) was investigated by ED, HREM, and XRD experiments. Figure 12a reproduces the most crowded section of the reciprocal space, which

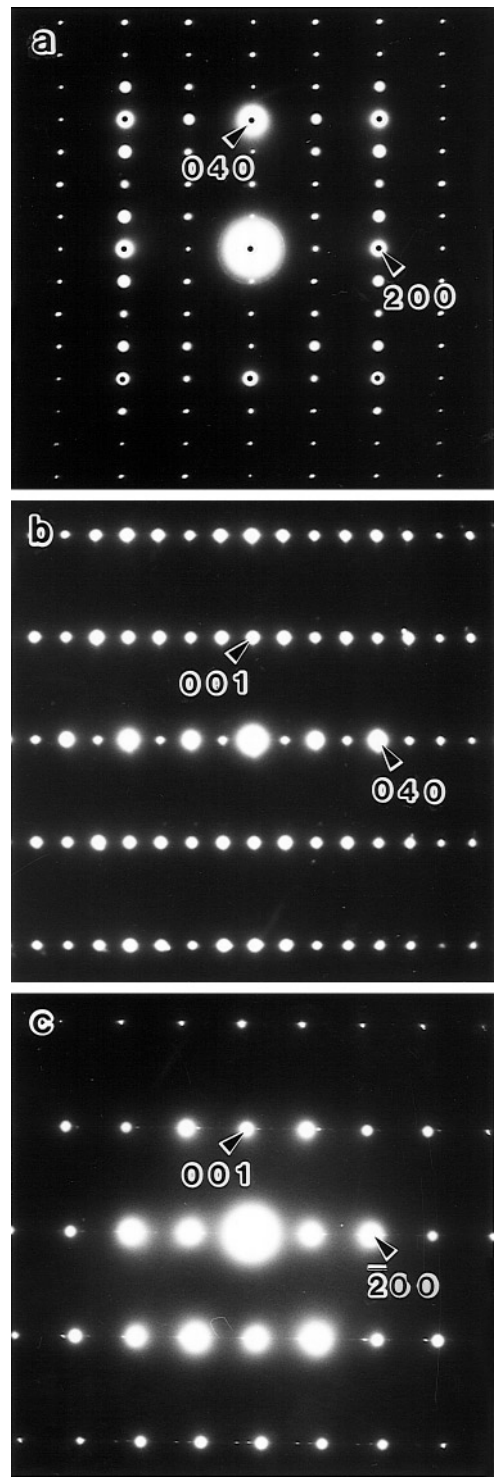

FIG. 12. Electron diffraction patterns of $CaCuO_2$ (II) with an incident beam along the c axis(a), a axis(b), and b axis(c).

reveals tetragonal arrays of intense spots (marked with dots) corresponding to $a_p/\sqrt{2} \times a_p/\sqrt{2} (\sim 2.7 \times 2.7\ \text{Å}^2)$ in the real space, where a_p represents the cell dimension of the primitive cubic perovskite. Since this tetragonal mesh is further divided into 2×4 arrays of weak diffraction spots, the actual unit cell dimensions of the basal plane are determined to be $a \approx \sqrt{2}a_p$ and $b \approx 2\sqrt{2}a_p$. Two other important ED patterns are shown in Figs. 12b and 12c. The pattern containing the b^* axis (12b) shows a rectangular arrangement of diffraction spots, whereas that containing the a^* axis (12c) shows an oblique arrangement. The c-axis length is 3.2 Å. Thus, the crystal system should be monoclinic. Tilting experiments about the a^* and the b^* axes were performed on several crystals and always showed a systematic splitting of diffraction spots. Typical examples are shown in Fig. 13. This small splitting must be due to twinning arising from the small monoclinic distortion. Moreover, tilting experiments about the b^* axis revealed a reflection condition of $k =$ even for $0k0$ reflections. The $0k0$ spots with $k =$ odd seen in Figs. 12a and 12b are due to the multiple diffraction effect. No other extinctions were observed. Thus, possible space groups to be considered are $P2_1$ (No. 4) or $P2_1/m$ (No. 11). Consistency with HREM images has led us to an assumption that the former noncentrosymmetric space group is more probable as described later. The basic crystal structure must be of the IL-type judging from the close relation of the unit-cell dimensions.

HREM images have allowed us to build a reasonable structural model. Figure 14a represents a typical HREM image taken with the incident electron beam parallel to the c axis. The arrangement of the dark dots in the image can be straightforwardly interpreted as representing the projected charge density, namely, as mapping the metal atoms because the image was obtained from a thin crystal edge near

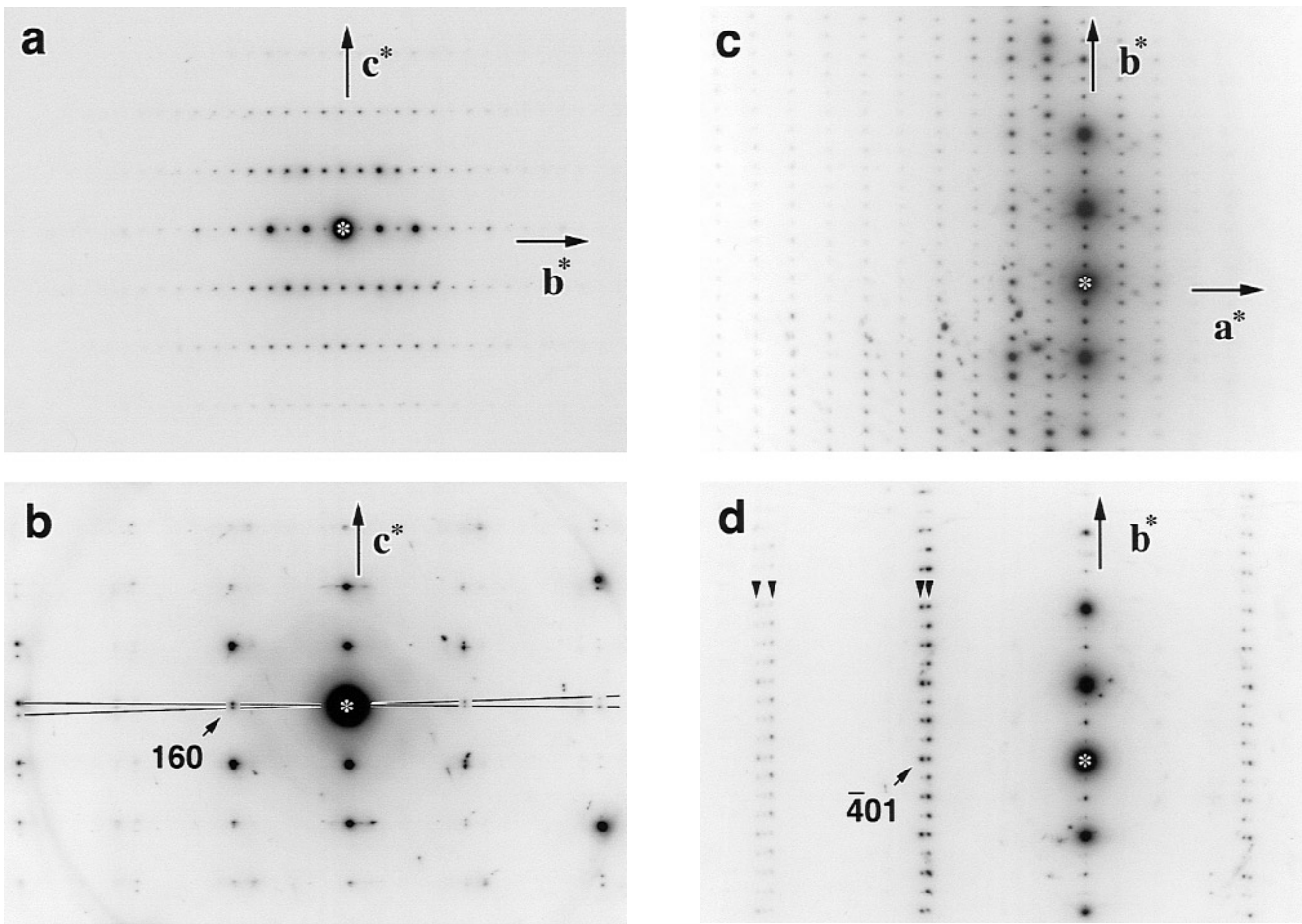

FIG. 13. Two series of ED patterns of $CaCuO_2$ (II). The contrast is inverted, showing each reflection as a dark spot. Rotating the crystal about the c^* axis by about 15° from the [100] zone axis (a) results in the [610] zone axis (b) where a systematic splitting of reflections along the c^* axis appears. This is because the a^* and c^* axes are not orthogonal to each other and also because the crystal consists of two structural variants related by twinning. A similar rotation of another crystal about the b^* axis by about 15° from nearly the [001] zone axis (c) results in the [104] zone axis (d) where a systematic splitting perpendicular to the b^* axis is seen. These experiments indicate that the crystals are twinned owing to the small monoclinic distortion, as often found in monoclinic crystals such as CuO.

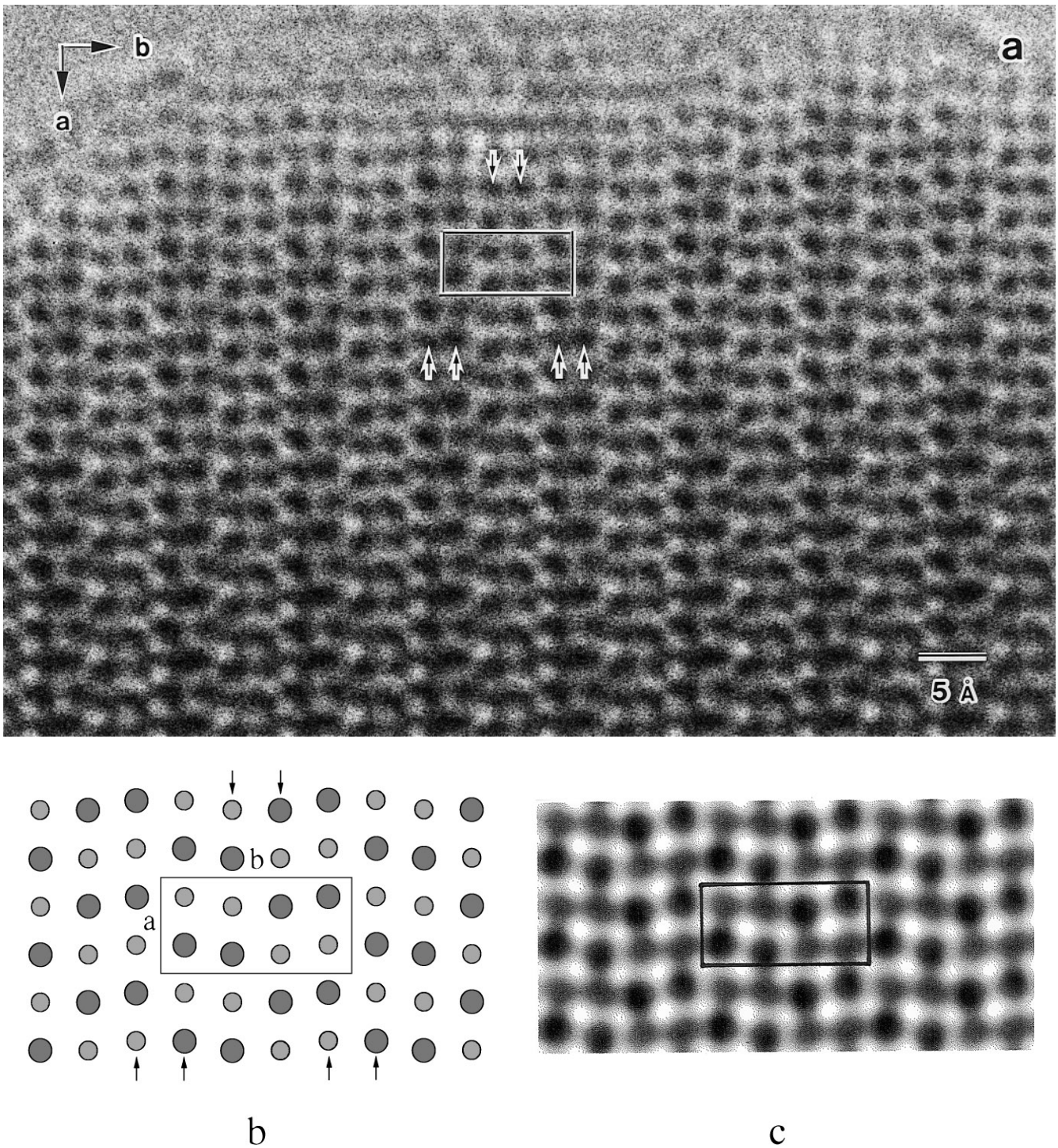

FIG. 14. (a) High-resolution image of $CaCuO_2$ (II) taken with an incident electron beam parallel to the *c* axis. Periodic arrangements of double rows of dark dots marked with arrows are seen. (b) Schematic representation of the dot pattern seen in the HREM image. (c) Computer-simulated image calculated using the atomic coordinates listed in Table 2.

the Scherzer defocus condition. One can see that double rows of metal ions (marked with arrows) which run along the *a* axis are aligned along the *b* axis. Each single row is made of alternating large and small dots and shifts half way to the other row as illustrated in Fig. 14b. Moreover, the relation between adjacent double rows is almost but not exactly out of phase. No mirror planes perpendicular to the *b* axis are found in the HREM image of Fig. 14a, suggesting

that $P2_1$ is more probable than $P2_1/m$. Assuming that the large and small dark dots represent Cu and Ca atoms, respectively, we have obtained a structural model where a pair of nearest neighboring CuO_4 squares share an edge and a pair of next-nearest neighbors share a corner. Based on this model, the lattice constants and some structure parameters were refined using a Rietveld analysis of the powder XRD pattern. The lattice constants obtained are $a = 5.4150(4)$ Å, $b = 10.7079(1)$ Å, $c = 3.1501(2)$ Å, and $\beta = 90.886(7)^\circ$. Observed and calculated interplane spacings are listed in Table 2. The monoclinic angle β is slightly smaller than that measured at the [010] ED pattern of Fig. 12c ($\sim 93^\circ$). However, it should be more accurate, because it was calculated from the systematic splitting of the $(1k1)$ and $(\bar{1}k1)$ ($k = 1, 3, 5$) reflections seen in the XRD pattern. The larger angle observed in the ED pattern may be due to the distortion of the lens system of the electron microscope. Other structural parameters could not be satisfactorily refined because of the presence of additional phases, but we believe that the assumed model was not far from the actual structure. A final determination of the structure would need high quality data to be obtained from a pure sample.

Here we have calculated a HREM image using the multislice method on the basis of the atomic coordinates obtained by the preliminary Rietveld analysis which are summarized in Table 3. The result is shown in Fig. 14c to be compared with Fig. 14a. A fairly good agreement is seen between the experimental and calculated images, which justify the model at least concerning the positions of metal atoms projected along the c axis.

TABLE 2
Powder X-Ray Diffraction Data of the Fundamental Reflections for Phase $CaCuO_2$(II)

Index	d_{obs} (Å)	d_{calc} (Å)	I_{obs}
110	4.832	4.826	26
120	3.807	3.804	1
001	3.150	3.146	14
200	2.707	2.703	1
040	2.677	2.677	100
$\bar{1}11$	2.655	2.652	19
210/111	2.622	2.621/2.619	39
$\bar{1}21$	2.437	2.438	45
121	2.414	2.412	33
140	2.400	2.399	3
$\bar{1}31$	2.173	2.172	33
230/131	2.155	2.155/2.154	75
150	1.991	1.991	1
240	1.902	1.902	50
$\bar{1}51$	1.687	1.687	11
250/151	1.678	1.679/1.678	27
$\bar{3}01$	1.575	1.574	3
$\bar{3}11$/301	1.555	1.558/1.553	4
061	1.553	1.552	1
311	1.538	1.537	5
$\bar{1}02$	1.515	1.517	2
102	1.506	1.504	2
$\bar{1}61$	1.494	1.495	8
161	1.491	1.489	5
042	1.357	1.356	9
080	1.338	1.339	12

TABLE 3
Atomic Coordinates Used for the HREM Image Simulation for $CaCuO_2$(II)

Atom	Site	x	y	z
Cu(1)	2*a*	0.725	0.130	0.089
Cu(2)	2*a*	0.775	0.370	0.089
Ca(1)	2*a*	0.193	0.114	0.536
Ca(2)	2*a*	0.307	0.386	0.536
O(1)	2*a*	0.974	0	0
O(2)	2*a*	0.474	0	0
O(3)	2*a*	0	0.251	0.042
O(4)	2*a*	0.5	0.251	0.042

Note. Space group, $P2_1$ (No. 4); $a = 5.4150(4)$ Å, $b = 10.7079(1)$ Å, $c = 3.1501(2)$ Å, $\beta = 90.886(7)^\circ$; $Z = 4$ formula unit per unit cell.

The structure model is illustrated in Fig. 15a. It is certainly closely related to the IL structure: As schematically shown in Fig. 15b, it can be led from the IL-type structure by dividing it into $\sqrt{2}\,a_p$ wide strips along the $[\bar{1}10]$ direction, each containing a zigzag chain of corner sharing CuO_4 squares, and then connecting them again after shifting every other strip by about $a_p/\sqrt{2}$ along the $[1\bar{1}0]$ direction, so that nearest-neighboring CuO_4 squares share edges. This way a connecting two CuO_4 planar squares by their edges is often seen in other cupric oxides like $Ca_{0.85}CuO_2$ (21). Judging from the small c axis length, there may be no oxygen atoms between these "CuO_2" planes. Thus, the crystal provides an alternative two-dimensional Cu–O network of which magnetic properties would be interesting. The density of $CaCuO_2$(II) is higher by about 4% than that of $CaCuO_2$(I).

It is also intriguing from the viewpoint of crystal chemistry to compare this structure with that of $SrCu_2O_3$ or $Sr_2Cu_3O_5$. In the case of these Sr cuprates the parent IL-type structure is divided into strips cut along the [100] direction, and these are combined again by edge-sharing. Thus, the major difference between the Ca and Sr cuprates just comes from the direction of cutting the IL-type structure.

CONCLUSION

We have studied the phase diagrams for the ternary system SrO–CaO–CuO at high pressure between 1.7 and 8 GPa. Phase relations among several high-pressure phases were determined. A new high-pressure phase $CaCuO_2$(II)

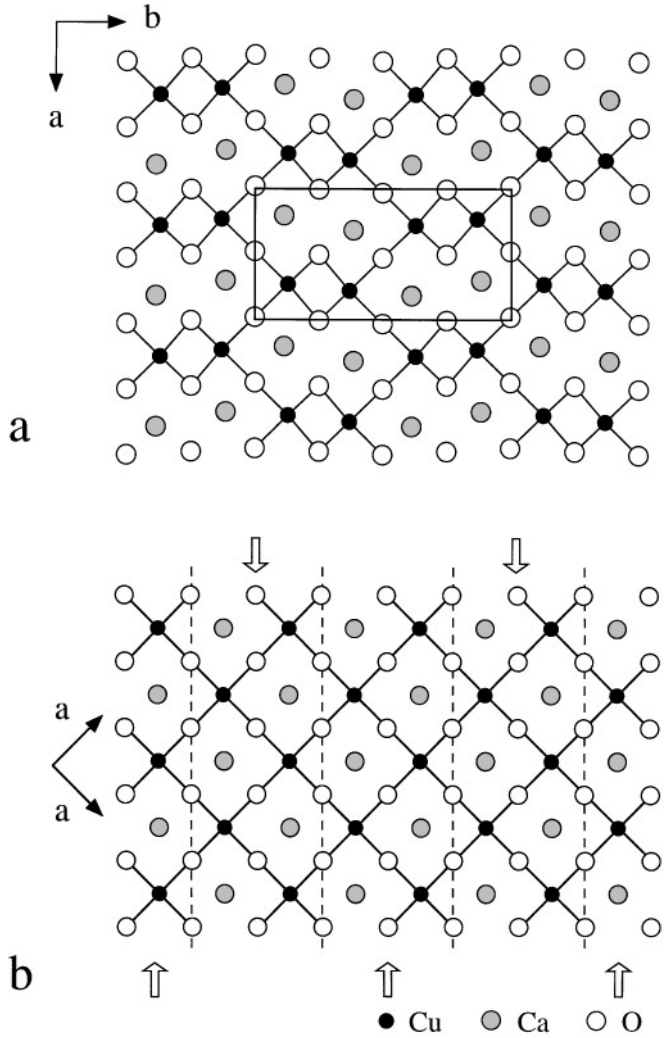

FIG. 15. (a) Structure model for $CaCuO_2$ (II) viewed along the *c* axis. A CuO_4 planar square shares an edge with the nearest-neighbor one and a corner with the next-nearest-neighbor one, so as to form a novel two-dimensional Cu–O network. The Ca atoms are located between the adjacent "CuO_2" planes. The rectangle shows the projected unit cell. (b) Schematic representation of the crystallographic relation to the IL structure. Dislocating the IL structure periodically by about $1/2 \cdot [1\bar{1}0]$ results in the structure shown in (a).

was found be stabilized at $P > 4.5$ GPa (1050°C). It is suggested that the structure of $CaCuO_2$(II) is closely related to the IL-type structure but contains a new type of Cu–O planes.

ACKNOWLEDGMENTS

The authors thank Y. Kusano and J. Takada for their help on the EDX analyses. This work has been supported by a Grant-in-Aid for Scientific Research on Priority Areas from the Ministry of Education, Science, and Culture, Japan and by CREST (Core Research for Evolutional Science and Technology) of Japan Science and Technology Corporation (JST).

REFERENCES

1. R. O. Suzuki, S. Kambara, H. Tsuchida, K. Shimizu, and K. Ono, "Advances in Superconductivity II, Proc. 2nd Int. Symp. Superconduct. (ISS'89)." p. 235, 1989.
2. R. S. Roth, C. J. Rawn, J. J. Ritter, and B. P. Burton, *J. Am. Ceram. Soc.* **72,** 1545 (1989).
3. K. Schulze, P. Majewski, B. Hettich, and G. Petzow, *Z. Metallkd.* **81,** 836 (1990).
4. M. Takano, Y. Ikeda, J. Takada, K. Oda, H. Kitaguchi, Y. Miura, Y. Tomii, and H. Mazaki, *Proc. Matter. Res. Soc., Int. Mtg. Adv. Mater.* 1 (1988).
5. C. L. Teske and H. Müller-Buschbaum, *Z. Anorg. Allg. Chem.* **371,** 325 (1969).
6. C. L. Teske and H. Müller-Buschbaum, *Z. Anorg. Allg. Chem.* **379,** 234 (1970).
7. T. Siegrist, S. Zahurak, D. Murphy, and R. S. Roth, *Nature* **334,** 231 (1988).
8. H. Yamane, Y. Miyazaki, and T. Hirai, *J. Cer. Soc. Jpn.* **97,** 143 (1989). [In Japanese]
9. T. Siegrist, R. S. Roth, C. J. Rawn, and J. J. Ritter, *Chem. Mater.* **2,** 192 (1990).
10. T. Siegrist, L. F. Scneemeyer, S. A. Sunshine, and J. V. Waszczak, *Mater. Res. Bull.* **23,** 1429 (1988).
11. M. Takano, Y. Takeda, H. Okada, M. Miysamoto, and T. Kusaka, *Physica C* **159,** 375 (1989).
12. Z. Hiroi, M. Azuma, M. Takano, and Y. Bando, *J. Solid State Chem.* **95,** 230 (1991).
13. E. Dagotto and T. M. Rice, *Science* **271,** 618 (1996).
14. Z. Hiroi, M. Azuma, M. Takano, and Y. Bando, *Physica C* **208,** 286 (1993).
15. F. Izumi, H. Asano, T. Ishigaki, E. Takayama-Muromachi, Y. Uchida, N. Watanabe, and T. Nishikawa, *Jpn. J. Appl. Phys.* **26,** 649 (1987).
16. Z. Hiroi, M. Takano, M. Azuma, and Y. Takeda, *Nature* **364,** 315 (1993).
17. C. L. Teske and H. Müller-Buschbaum, *Z. Anorg. Allg. Chem.* **370,** 134 (1969).
18. O. Milat, G. V. Tendeloo, S. Amelinckx, T. Babu, and C. Greaves, *Solid State Comm.* **79,** 1059 (1991).
19. J. Karpinski, I. Mangelschots, H. Schwer, K. Conder, A Morawski, T. Lada, and A. Paszewin, *Physica C* **235–240,** 917 (1994).
20. J. Karpinski, H. Schwer, I. Mangelschots, K. Conder, A Morawski, T. Lada, and A. Paszewin, *Physica C* **234,** 10 (1994).
21. T. G. N. Babu and C. Greaves, *Mater. Res. Bull.* **26,** 499 (1991).